Biodistribution and Radiation Dosimetry for the Tau Tracer ^{18}F-THK-5351 in Healthy Human Subjects

Ing-Tsung Hsiao*[1–3], Kun-Ju Lin*[1–3], Kuo-Lun Huang[4], Chin-Chang Huang[4], Han-Shiuan Chen[2], Shiaw-Pyng Wey[1,2], Tzu-Chen Yen[1,2,3], Nobuyuki Okamura[5,6], and Jung-Lung Hsu[4,7]

[1]Department of Nuclear Medicine and Center for Advanced Molecular Imaging and Translation, Chang Gung Memorial Hospital, Taoyuan, Taiwan; [2]Healthy Aging Research Center and Department of Medical Imaging and Radiological Sciences, Chang Gung University, Taoyuan, Taiwan; [3]Neuroscience Research Center, Chang Gung Memorial Hospital, Taoyuan, Taiwan; [4]Department of Neurology, Chang Gung Memorial Hospital and Chang Gung University, Taoyuan, Taiwan; [5]Division of Neuroimaging, Institute of Development, Aging, and Cancer, Tohoku University, Sendai, Japan; [6]Department of Pharmacology, Faculty of Medicine, Tohoku Medical and Pharmaceutical University, Sendai, Japan; and [7]Graduate Institute of Humanities in Medicine, Taipei Medical University, Taipei, Taiwan

^{18}F-THK-5351 is a novel radiotracer that demonstrates high binding selectivity and affinity for tau pathology and exhibits better pharmacokinetics in the living brain than previous THK tau probes. The aim of the present study was to estimate the radiation dose of ^{18}F-THK-5351 in humans and to compare the clinical radiation dosimetry results to estimations published previously with preclinical data. **Methods:** Serial whole-body PET/CT imaging was performed for 240 min on 12 healthy volunteers after injecting ^{18}F-THK-5351 (mean administered activity, 377.8 ± 14.0 MBq; range, 340–397 MBq). The bladder and gallbladder were delineated on PET images, and the other organs were delineated on CT images. Voided urine activity was recorded. The decay-corrected and normalized ^{18}F-THK-5351 activity of 15 source-organ regions as a function of time was entered into the OLINDA/EXM software to calculate the effective dose for each subject following the medical internal radiation dosimetry schema. **Results:** Overall, the ^{18}F-THK-5351 injection was well tolerated. The highest mean initial uptake at 10 min after injection was in the liver (11.4% ± 2.0%), lung (5.7% ± 2.1%), intestine (3.4% ± 0.8%), and kidney (1.4% ± 0.3%). The highest mean absorbed dose of radiation was in the gallbladder wall (242.2 ± 105.2 μGy/MBq), upper large intestine (90.0 ± 15.8 μGy/MBq), small intestine (79.5 ± 13.8 μGy/MBq), and liver (55.8 ± 6.1 μGy/MBq). The resultant whole-body effective dose was 22.7 ± 1.3 μSv/MBq. **Conclusion:** Our results suggest that a routine injection of 370 MBq of ^{18}F-THK-5351 would lead to an estimated effective dose of 8.4 mSv; hence, ^{18}F-THK-5351 has a radiation burden similar to that of other commonly used clinical tracers. Our findings in humans were compatible with recently published preclinical dosimetry data extrapolated from mice.

Key Words: ^{18}F-THK-5351; Alzheimer's disease; tau; whole body biodistribution; radiation dosimetry

J Nucl Med 2017; 58:1498–1503
DOI: 10.2967/jnumed.116.189126

Alzheimer disease (AD) is the most common type of dementia. The hallmark pathology of this disease involves the accumulation of β-amyloid plaques and tau proteins (*1,2*). In addition, spatial spreading of these biomarkers is indicative of the temporal progression of AD (*3,4*).

Fortunately, the rapid development of molecular imaging techniques and tracers has permitted early detection and diagnosis of AD (*5*). One of the earliest successfully introduced tracers in clinical studies was Pittsburgh compound B, which binds to amyloid with low nanomolar affinity (*6*). Since then, more widely distributable tracers labeled with ^{18}F, including ^{18}F-flutemetamol, ^{18}F-florbetaben, and ^{18}F-florbetapir, have been approved for assessing the presence of amyloid plaques in clinical settings and have encouraged researchers to perform clinical trials aimed at developing novel therapeutic strategies (*7*).

However, β-amyloid plaques initially develop in preclinical AD, and the amyloid burden, as imaged with PET, does not appear to correlate with the clinical symptoms of late mild cognitive impairment and AD (*8–11*). On the other hand, tau aggregation, in the form of neurofibrillary tangles, which first appear in the mesial temporal region and then spread to the neocortex, is associated with the clinical stage of AD (*11,12*). In this regard, noninvasive imaging of tau could potentially facilitate early diagnosis of AD, help differentiate it from other dementing disorders, and allow researchers to evaluate the outcomes of tau immunization therapies (*13*).

Given the potential of radiotracers for imaging tau protein in the brain, researchers have been focused on developing them (*14–19*). Because tau aggregates are mainly intracellular and may coexist with amyloid plaques, the success of in vivo human imaging relies on the ability of the radiotracer to cross the blood–brain barrier with high selectivity for the target. Some of the proposed tau tracers have met these criteria and are currently undergoing clinical assessments, including the THK analogs ^{18}F-THK-5105, ^{18}F-THK-5117 (*16*), ^{11}C-PBB3 (*17*), and ^{18}F-AV-1451 (formerly called ^{18}F-T807) (*19*). However, tracers such as ^{18}F-THK-5117 showed relatively high nonspecific uptake in the subcortical white matter, which might hinder the visual interpretation of PET images. To reduce nonspecific tracer retention in the white matter, Harada et al. (*20*) developed a novel tau PET tracer, ^{18}F-THK-5351, by replacing a benzene

Received Dec. 28, 2016; revision accepted Mar. 13, 2017.
For correspondence or reprints contact: Jung-Lung Hsu, Department of Neurology, Chang Gung Memorial Hospital and Chang Gung University, No. 5, Fuxing St., Guishan District, Taoyuan City 333, Taiwan.
E-mail: tulu@ms36.hinet.net
*Contributed equally to this work.
Published online Mar. 23, 2017.

ring of ^{18}F-THK-5117 with pyridine. The preliminary data showed faster kinetics, higher contrast, and lower retention in the subcortical white matter for ^{18}F-THK-5351 than for ^{18}F-THK-5117 (*20*). However, the internal radiation dosimetry data for ^{18}F-THK-5351 have not yet been published.

In the present study, we aimed to estimate the radiation dose of ^{18}F-THK-5351 to the whole body and various organs in humans. We intravenously injected ^{18}F-THK-5351 into 12 healthy human volunteers and performed organ time–activity measurements with whole-body PET images to define the tissue concentration of the injected radiotracer. Then, the absorbed doses were estimated, and the effective doses were calculated with the medical internal radiation dosimetry method using the OLINDA software (Vanderbilt University) by modifying the standard reference phantoms with subject-specific masses.

MATERIALS AND METHODS

Subjects

Twelve healthy control subjects were recruited for this study (age range, 34–54 y; 7 men and 5 women; Table 1). None of the subjects demonstrated any clinically significant abnormalities during their physical or neurologic examinations. All subjects' laboratory investigation results were within the reference range. Safety data, including vital signs, electrocardiograms, and laboratory parameters, were collected before and at 5 h after injection for comparison. The study was approved by the Institutional Review Board at Chang Gung Memorial Hospital. Informed written consent was obtained from all subjects after they had received a detailed explanation of the study. The trial was registered with clinicaltrials.gov (NCT02686216).

Preparation of ^{18}F-THK-5351

The radiotracer was synthesized using the methods of Harada et al. (*20*), with slight modifications. Our modifications included using less precursor (1 mg instead of 3 mg) and adding sodium ascorbate (0.5% w/v) in the mobile phase of high-performance liquid chromatography purification to prevent radiolysis of the product. In brief, ^{18}F-THK-5351 was prepared from its tosylate precursor, (*S*)-2-(2-methylaminopyrid-5-yl)-6-[[2-(tetrahydro-2H-pyran-2-yloxy)-3-tosyloxy] propoxy] quinoline (THK-5352), according to a previously described method for synthesizing ^{18}F-THK-5105 and ^{18}F-THK-5117 (*16*). ^{18}F-THK-5351 was purified using semipreparative high-performance liquid chromatography (column: Inertsil ODS-4 [GL Sciences, Inc.]; mobile phase: 20 mM NaH_2PO_4/acetonitrile [75:25]; flow rate: 5.0 mL/min). ^{18}F-THK-5351 was obtained at a radiochemical yield of 30% ± 4% (decay-corrected) with a radiochemical purity of more than 95% and specific activity of 178.8 ± 32.1 TBq/mmol (n = 8). The radiotracer was formulated in a saline solution containing ethanol (7%), sodium ascorbate (0.5%), and polysorbate-80 (0.15%) for clinical evaluation.

TABLE 1
Demographics of Study Subjects

Subject no.	Sex	Age (y)	Mass (kg)	ID (MBq)
1	M	52	53	389
2	M	49	54	377
3	F	47	53	397
4	F	45	53	340
5	M	47	59	388
6	F	48	70	379
7	M	46	65	370
8	F	39	65	376
9	M	38	97	382
10	M	38	76	383
11	M	34	100	374
12	M	54	73	379
Mean ± SD		44.8 ± 6.2	68.2 ± 16.3	377.8 ± 14.0

ID = injected dose.

Whole-Body and Brain PET Imaging

Serial PET scans of the whole body were acquired on a dedicated PET/CT scanner (Siemens Biograph mCT 16; Siemens Medical Solutions). Low-dose CT scans for attenuation correction were acquired with the following parameters: 40 mAs, 120 keV, 512 × 512 matrix, 5-mm slice thickness, 201 slices, 30 mm/s increments, 0.5-s rotation time, and pitch of 0.8. The imaging field ranged from the head to the proximal thighs. The ^{18}F-THK-5351 radiotracer was injected through a venous line into the arm of 12 subjects, with a mean administered activity of 377.8 ± 14.0 MBq. The scanning protocol included 1- to 2-min emission scans for 4 cycles at 10, 60, 120, and 240 min after injection. Each cycle consisted of 7 bed positions; thus, the whole-body scanning time was 10 min per cycle. Additional dynamic brain scans were acquired between the whole-body scanning sessions, ranging from 0 to 10 min, 20 to 60 min, and 70 to 90 min after injection. Subjects were allowed to leave the scanner before the third and fourth whole-body scans. Before the third and fourth emission imaging sessions, additional whole-body CT attenuation correction scans were acquired. All data were decay-corrected to the starting time of each individual scan. All PET images were corrected for photon attenuation, dead time, random events, and scatter. Images were reconstructed in the 3-dimensional mode using a manufacturer-supplied reconstruction technique (ordered-subsets expectation maximization with 16 subsets and 2 iterations).

Uptake of ^{18}F-THK-5351 in the target organs was determined by calculating the SUV according to the following formula:

$$\mathrm{SUV} = \frac{\text{decay-corrected tissue activity (Bq/mL)}}{\text{injected dose (Bq)/body weight (g)}}. \qquad \text{Eq. 1}$$

The $\mathrm{SUV}_{\mathrm{mean}}$ of each organ of interest at time t after injection, that is, $\overline{\mathrm{SUV}}_{\mathrm{organ}}(t)$, was assessed in all subjects.

Dosimetry

Full organ segmentation was performed manually on CT and PET images for the entire body and each visualized organ (brain, salivary gland, thyroid, lung, liver, gallbladder, heart, kidneys, spleen, and bladder) using the PMOD image analysis software, version 3.2 (PMOD Technologies Ltd.). Bone marrow dosimetry was derived from CT-based volumes of interest that were placed over lumbar vertebrae 2–4. All volumes of interest were drawn subjectively around each organ by an experienced nuclear medicine physician. The $\mathrm{SUV}_{\mathrm{mean}}$ from each target was then converted to the percentage injected dose (%ID), using the known mass of an organ or its contents, as follows:

$$\%\mathrm{ID}(t) = 100\% \times \overline{\mathrm{SUV}}_{\mathrm{organ}}(t) \times \frac{\mathrm{V}_{\mathrm{organ}}}{\mathrm{M}_{\mathrm{body}}}, \qquad \text{Eq. 2}$$

where %ID (t), $\mathrm{V}_{\mathrm{organ}}$, and $\mathrm{M}_{\mathrm{body}}$ are the %ID measured at time t after injection, the volume of the organ (mL), and the mass (g) of the whole

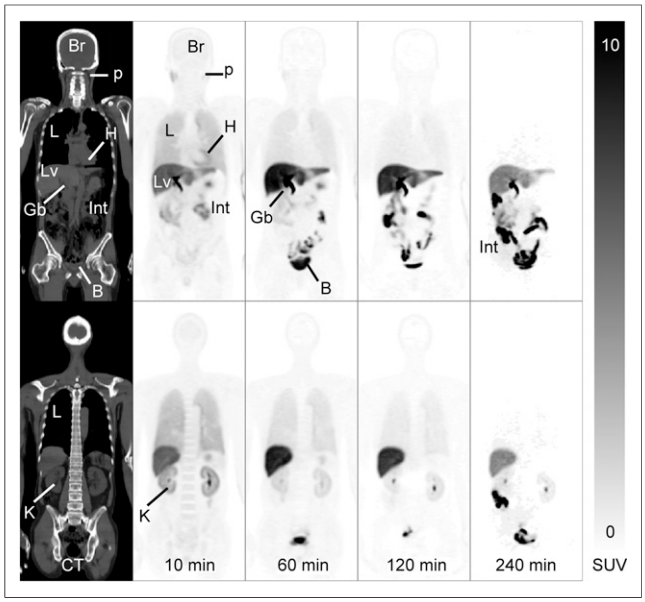

FIGURE 1. ^{18}F-THK-5351 PET/CT images of healthy 53-y-old woman. On right are coronal sequential whole-body PET images (75 mm thick) at 10, 60, 120, and 240 min after ^{18}F-THK-5351 injection; on left are corresponding CT images. Scale represents SUV. B = bladder; Br = brain; Gb = gallbladder; H = heart; Int = intestine; K = kidney; L = lung; Lv = liver; p = parotid gland.

body, respectively. Time–activity curves for the organs were fit to a nonlinear regression model of exponential uptake and clearance using the OLINDA/EXM software. For organs without an exponential curve pattern, such as the gallbladder, the area under the curve was calculated from the available time–activity curve via the trapezoidal rule method. For a conservative analysis, the activity after the last time point was considered radioactivity decay. The residence times for the bowel and bladder were calculated using the ICRP 30 gastrointestinal model and dynamic bladder model, respectively, as incorporated in OLINDA. In the bladder model, the maximum cumulated activity of the urinary bladder content was determined by fitting the bladder time–activity curve with an exponential growth function. A remainder term was computed for activity in the body that was not specifically visualized in an organ (1 − all specific organs). Residence times were input into the OLINDA/EXM software for each organ on the basis of the adult model; we also modified the standard reference phantoms with subject-specific masses to compute the individual organ doses and effective dose equivalent (*21*). The OLINDA/EXM software multiplies the residence time for each subject and organ by the S value (mSv/MBq × h) to obtain the dose, as follows:

$$\text{Dose (mSv/MBq)} = \text{residence time (h)} \times \text{S value}. \qquad \text{Eq. 3}$$

S values are implemented within the OLINDA/EXM software.

RESULTS

The ^{18}F-THK-5351 injection was safe and tolerable, and no immediate adverse events were observed. No significant changes in the subjects' vital signs (heart rate, blood pressure, and respiratory rate); electrocardiograms; and laboratory parameters, including serum chemistry and hematology, were noted after injection. The whole-body images from a representative subject are presented in Figure 1. Uptake of the radiotracer in the lung, kidney, and blood-containing organs occurred within 10 min after injection, followed by rapid clearance. Prominent liver and gallbladder uptake occurred at 60 min after injection, followed by a gradual decrease over the remainder of the study (Fig. 1). The bladder and bowel showed substantial uptake from 10 min until the end of the study because of urine accumulation and radioactivity elimination through the gastrointestinal tract.

The time–activity curves of the decay-corrected %ID of each organ for all 12 subjects are shown in Figure 2, and the specific values are listed in Supplemental Table 1 (supplemental materials are available at http://jnm.snmjournals.org). The time–activity curves showed high initial uptake of the radiotracer in the liver and lung, with values of 11.4 ± 2.0 and 5.7 ± 2.1 %ID, respectively. The organs with a fast wash-in and washout were the lungs, kidneys, heart, and thyroid. In contrast, uptake and washout in the brain, bone marrow, and liver were gradual. Uptake in the brain was 1.0 ± 0.2 %ID at 10 min after radiotracer injection. The maximum radioactivity that accumulated in the urinary bladder was calculated as 4.9 ± 3.3 %ID, with a biologic half-life of 1.1 ± 0.6 h (exponential growth curve–fitting result from the biodistribution data). The residence times or the average number of disintegrations was then calculated using the area under the fitting curves in the source organs (Supplemental Table 2). Table 2 presents the dosimetry data, including the effective dose equivalents for various organs in the 12 subjects. The mean

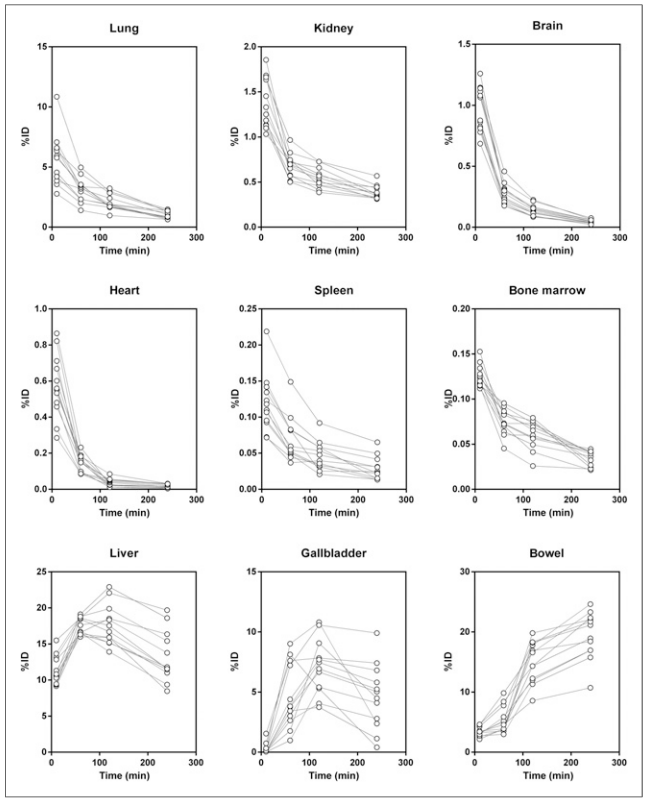

FIGURE 2. Fractional activity in various organs with respect to total-body activity (%ID) for 12 subjects.

TABLE 2
Dosimetry for ^{18}F-THK-5351 from 12 Subjects

Parameter/organ	μGy/MBq (mean)	mrad/mCi (mean)	CV (%)
Adrenals	15.9	589.0	5.0
Brain	2.9	10.8	10.7
Breasts	8.6	31.7	11.7
Gallbladder	242.2	896.3	43.4
Lower large intestine	34.6	128.2	14.8
Small intestine	79.5	294.0	17.4
Stomach	18.4	68.2	6.4
Upper large intestine	90.0	333.0	17.5
Heart	10.3	38.2	6.4
Kidneys	20.9	77.5	8.4
Liver	55.8	206.6	10.9
Lungs	17.4	64.2	19.0
Muscle	11.4	42.0	9.3
Ovaries (n = 4)	21.7	80.1	11.1
Pancreas	17.9	66.4	5.2
Bone marrow	11.7	43.1	8.2
Osteogenic cells	15.4	56.8	14.2
Skin	8.0	29.6	12.7
Spleen	8.8	32.6	5.8
Testes (n = 8)	8.8	32.5	13.0
Thymus	10.0	36.9	11.3
Thyroid	5.7	21.1	10.5
Urinary bladder	42.4	156.8	29.2
Uterus	21.0	77.5	14.8
Total body	14.5	53.5	18.9
Effective dose equivalent	41.6*	153.9†	16.4
Effective dose	22.7*	84.0†	5.8

*μSv/MBq.
†mrem/mCi.
CV = coefficient of variation calculated as (SD/mean) × 100%.
Data are for urinary bladder clearance model with 4.8-h voiding intervals.

effective dose for the 4.8-h bladder-voiding model was 22.7 ± 1.3 μSv/MBq.

Dynamic brain images at 0, 10, 50, 120, and 240 min after injection are shown in Figure 3. The early-phase brain image was averaged from the 0- to 10-min dynamic brain scan, whereas the other brain images were reconstructed from the whole-body scans. These serial 10-min brain scans of healthy subjects demonstrate that images of adequate quality can be acquired with a 370-MBq (10-mCi) injection. The early-phase (0–10 min) brain image shows a perfusionlike distribution of radiotracer with cortical and subcortical uptake, as expected. As for the brain, the SUVs at 10 min after injection were the highest in the striatum (1.95 ± 0.51), followed by the medial temporal (1.42 ± 0.33), frontal (1.23 ± 0.35), and parietal (1.14 ± 0.30) regions and the cerebellum (1.13 ± 0.30). Ten minutes after injection, the radiotracer had washed out quickly from most of the brain regions except the basal ganglia, thalamus, medial temporal region, and midbrain areas, which showed substantial retention of the radioactivity. In the late phase (after 50 min), no definite retention or uptake of radioactivity was noted in the brain except for blood-pool activity in the internal carotid artery.

DISCUSSION

To the best of our knowledge, this study was the first human clinical trial to directly evaluate the biodistribution and whole-body radiation dosimetry of ^{18}F-THK-5351. The ^{18}F-THK-5351 biodistribution was dominated by activity in the hepatobiliary system, with little renal clearance. The highest doses were in the gallbladder (242.2 ± 105.2 μGy/MBq), upper large intestine (90.0 ± 15.8 μGy/MBq), small intestine (79.5 ± 13.8 μGy/MBq), and liver (55.8 ± 6.1 μGy/MBq). The dosimetry data showed that to avoid exceeding a 50-mGy dose to the critical organ—the liver—the maximum injected dose that can be used in a ^{18}F-THK-5351 study is 896 MBq (24.2 mCi). The estimated effective dose was 22.7 μSv/MBq, which is in the same range (20–30 μSv/MBq) as that for other ^{18}F-labeled radiopharmaceuticals. For a routine injected dose of 175 MBq (5 mCi), or a higher dose of 370 MBq for research purposes, the whole-body doses are estimated to be 4.2 and 8.3 mSv, respectively, which are well below the whole-body dose limit of 30 mSv (single dose) specified by the Food and Drug Administration for research subjects (*22*).

When comparing our human data with data derived by harvesting organs from mice, we found that the initial distribution of radioactivity seemed similar, showing dominant hepatobiliary uptake (*20*). However, clearance of the radiotracer from the liver and lung was much faster in mice than in humans, and the absorbed doses calculated with the extrapolation method for the liver and lung were underestimated by factors of 5 and 2, respectively, compared with our clinical values (9.4 vs. 55.8 μGy/MBq for the liver and 8.0 vs. 17.4 μGy/MBq for the lung). This discrepancy is generally related to interspecies differences in metabolism. Although the mouse-derived measurement was roughly comparable to the human-derived dose (18.4 vs. 22.7 μSv/MBq), considerable differences in the critical organ dose estimates and pharmacokinetics were found for this novel radiotracer. In this regard, for investigating the biodistribution of ^{18}F-THK-5351, initial evaluations using human whole-body imaging instead of animal data alone are desirable before wide clinical application of this tracer (*23*).

In the present study, high variability (variation coefficient > 20%) in the measured residence time and estimated absorbed doses was found in the gallbladder and urinary bladder wall. Because we did not limit the subjects' intake of food or water before or during the study period, this high variability was most likely related to differences in the functional clearance rate among subjects.

As observed in our dynamic brain images, substantial radioactivity was retained in the basal ganglia. Although tau pathology has been reported in the basal ganglia of individuals with AD (*24*), data on the striatal uptake of ^{18}F-THK-5351 from in vitro autoradiography and binding assays are limited and

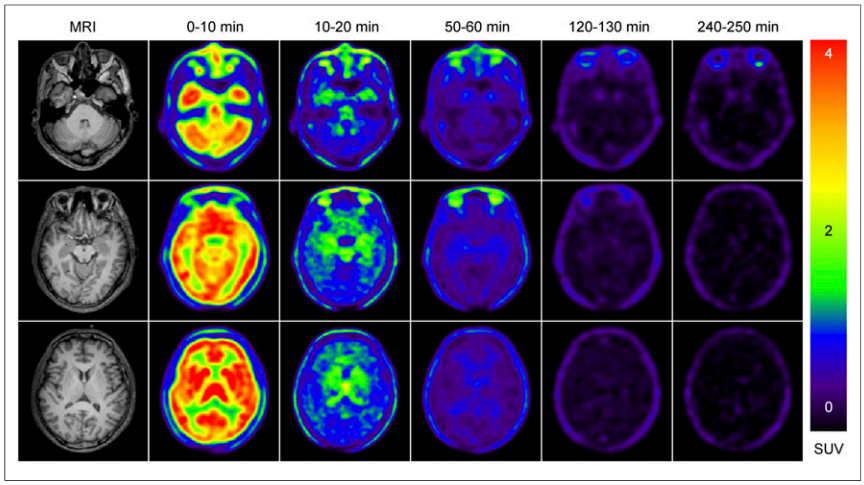

FIGURE 3. ^{18}F-THK-5351 PET and MR brain images of 47-y-old woman. On left are structural MR images; on right are PET images acquired in early (0–10 min), mid (10–20 min), and late (after 50 min) phases after ^{18}F-THK-5351 injection. Color scale represents SUV.

inconclusive (*20,25*). This substantial radioactivity retention in the basal ganglia may also be related to off-target binding, as suggested by studies on other tau-seeking radiotracers, such as AV-1451 (*26*). However, despite the potential for off-target binding in subcortical structures, retention in the choroid plexus and venous sinus was not significantly higher for ^{18}F-THK-5351 than for ^{18}F-AV-1451, as agrees with the findings of a previous report (*20*).

One limitation of our biodistribution study was the lack of later time points. That type of study was difficult to perform because our Radiation Safety Committee and Institutional Review Board asked us to minimize the radiation exposure for research purposes; thus, we omitted the time point at 4 h after injection to reduce the need for an additional attenuation-correction CT dose. For organs that do not fit the exponential decay curve, the remaining radioactivity in each organ was conservatively assumed to be removed through physical decay only after the last measured time point. In addition, since the whole-body images were collected using multiple bed positions, the exact acquisition time points for individual organs would likely not be the same as those estimated in our study. These subtle timing differences may affect the time–activity curve of each organ and the final estimates of the absorbed radiation doses. Another limitation was that the mean age of the subjects was relatively lower than that of the general-dementia target group. Thus, the possibility of heterogeneous biodistributions at different ages cannot be excluded.

CONCLUSION

The present whole-body biodistribution study demonstrated that a routine 370-MBq injection of ^{18}F-THK-5351 would lead to an estimated effective dose of 8.4 mSv. Importantly, ^{18}F-THK-5351 showed a radiation burden similar to that of other widely used clinical tracers. Our results in humans were compatible with recently published preclinical dosimetry data extrapolated from mice, although some differences in the individual organ dose estimates and pharmacokinetics were noted for the lung and liver. The radiation risk profile we identified suggests that in a single year, a subject could safely receive multiple injections of ^{18}F-THK-5351 either alone or in conjunction with other brain radiotracers.

DISCLOSURE

This study was supported by grants from the Chang Gung Memorial Hospital Research Fund (CMRPG3E1451, CMRPG3B0311, CMRPD1E0302, 103-2314-B-182-010-MY3, and CIRPG3D0092) and from the Ministry of Science and Technology, Taiwan (NSC 102-2314-B-182-049-MY3 and MOST 104-2314-B-182A-083-MY2). No other potential conflict of interest relevant to this article was reported.

ACKNOWLEDGMENTS

We gratefully acknowledge Cheng-Hsiang Yao for preparing the radiotracer and Wu Chia-Hui for assisting with image analysis. This study was presented in part at the Alzheimer's Association International Conference (AAIC) 2016 held in Toronto, Ontario, Canada.

REFERENCES

1. Hardy J, Selkoe DJ. The amyloid hypothesis of Alzheimer's disease: progress and problems on the road to therapeutics. *Science.* 2002;297:353–356.
2. Alonso AC, Grundke-Iqbal I, Iqbal K. Alzheimer's disease hyperphosphorylated tau sequesters normal tau into tangles of filaments and disassembles microtubules. *Nat Med.* 1996;2:783–787.
3. Arnold SE, Hyman BT, Flory J, Damasio AR, Van Hoesen GW. The topographical and neuroanatomical distribution of neurofibrillary tangles and neuritic plaques in the cerebral cortex of patients with Alzheimer's disease. *Cereb Cortex.* 1991;1:103–116.
4. Braak H, Braak E. Staging of Alzheimer's disease-related neurofibrillary changes. *Neurobiol Aging.* 1995;16:271–278.
5. McKhann GM, Knopman DS, Chertkow H, et al. The diagnosis of dementia due to Alzheimer's disease: recommendations from the National Institute on Aging-Alzheimer's Association workgroups on diagnostic guidelines for Alzheimer's disease. *Alzheimers Dement.* 2011;7:263–269.
6. Klunk WE, Engler H, Nordberg A, et al. Imaging brain amyloid in Alzheimer's disease with Pittsburgh Compound-B. *Ann Neurol.* 2004;55:306–319.
7. Sevigny J, Chiao P, Bussière T, et al. The antibody aducanumab reduces Aβ plaques in Alzheimer's disease. *Nature.* 2016;537:50–56.
8. Lin K-J, Hsiao T, Hsu J-L, et al. Imaging characteristic of dual-phase ^{18}F-florbetapir (AV-45/Amyvid) PET for the concomitant detection of perfusion deficits and beta-amyloid deposition in Alzheimer's disease and mild cognitive impairment. *Eur J Nucl Med Mol Imaging.* 2016;43:1304–1314.
9. Jack CR, Wiste HJ, Lesnick TG, et al. Brain β-amyloid load approaches a plateau. *Neurology.* 2013;80:890–896.
10. Huang KL, Lin KJ, Hsiao IT, et al. Regional amyloid deposition in amnestic mild cognitive impairment and Alzheimer's disease evaluated by [^{18}F]AV-45 positron emission tomography in Chinese population. *PLoS One.* 2013;8:e58974.
11. Arriagada PV, Growdon JH, Hedley-Whyte ET, Hyman BT. Neurofibrillary tangles but not senile plaques parallel duration and severity of Alzheimer's disease. *Neurology.* 1992;42:631–639.
12. Bierer LM, Hof PR, Purohit DP, et al. Neocortical neurofibrillary tangles correlate with dementia severity in Alzheimer's disease. *Arch Neurol.* 1995;52:81–88.
13. Wang L, Benzinger TL, Su Y, et al. Evaluation of tau imaging in staging Alzheimer disease and revealing interactions between β-amyloid and tauopathy. *JAMA Neurol.* 2016;73:1070–1077.

14. Small GW, Kepe V, Huang SC, et al. P2-206 in vivo brain imaging of tau aggregation in frontal temporal dementia using [F-18]FDDNP positron emission tomography [abstract]. *Neurobiol Aging.* 2004;25(suppl):S288–S289.
15. Shao X, Carpenter GM, Desmond TJ, et al. Evaluation of [^{11}C]N-methyl lansoprazole as a radiopharmaceutical for PET imaging of tau neurofibrillary tangles. *ACS Med Chem Lett.* 2012;3:936–941.
16. Okamura N, Furumoto S, Harada R, et al. Novel ^{18}F-labeled arylquinoline derivatives for noninvasive imaging of tau pathology in Alzheimer disease. *J Nucl Med.* 2013;54:1420–1427.
17. Hashimoto H, Kawamura K, Igarashi N, et al. Radiosynthesis, photoisomerization, biodistribution, and metabolite analysis of ^{11}C-PBB3 as a clinically useful PET probe for imaging of tau pathology. *J Nucl Med.* 2014;55:1532–1538.
18. Zimmer ER, Leuzy A, Gauthier S, Rosa-Neto P. Developments in tau PET imaging. *Can J Neurol Sci.* 2014;41:547–553.
19. Chien DT, Bahri S, Szardenings AK, et al. Early clinical PET imaging results with the novel PHF-tau radioligand [F-18]-T807. *J Alzheimers Dis.* 2013;34:457–468.
20. Harada R, Okamura N, Furumoto S, et al. ^{18}F-THK5351: a novel PET radiotracer for imaging neurofibrillary pathology in Alzheimer disease. *J Nucl Med.* 2016;57:208–214.
21. Stabin MG, Sparks RB, Crowe E. OLINDA/EXM: the second-generation personal computer software for internal dose assessment in nuclear medicine. *J Nucl Med.* 2005;46:1023–1027.
22. Guidance for industry and researchers: the Radioactive Drug Research Committee—human research without an investigational new drug application. U.S. Food and Drug Administration website. http://www.fda.gov/downloads/drugs/guidancecomplianceregulatoryinformation/guidances/ucm163892.pdf. Published August 2010. Accessed June 27, 2017.
23. Sakata M, Oda K, Toyohara J, Ishii K, Nariai T, Ishiwata K. Direct comparison of radiation dosimetry of six PET tracers using human whole-body imaging and murine biodistribution studies. *Ann Nucl Med.* 2013;27:285–296.
24. Braak H, Braak E. Alzheimer's disease: striatal amyloid deposits and neurofibrillary changes. *J Neuropathol Exp Neurol.* 1990;49:215–224.
25. Lemoine L, Saint-Aubert L, Marutle A, et al. Visualization of regional tau deposits using ^{3}H-THK5117 in Alzheimer brain tissue. *Acta Neuropathol Commun.* 2015;3:40.
26. Lowe VJ, Curran G, Fang P, et al. An autoradiographic evaluation of AV-1451 tau PET in dementia. *Acta Neuropathol Commun.* 2016;4:58.